

# Template for Preparation of Manuscripts for *Nano Research*

This template is to be used for preparing manuscripts for submission to *Nano Research*. Use of this template will save time in the review and production processes and will expedite publication. However, use of the template is not a requirement of submission. Do not modify the template in any way (delete spaces, modify font size/line height, etc.). If you need more detailed information about the preparation and submission of a manuscript to Nano Research, please see the latest version of the Instructions for Authors at <http://www.thenanoresearch.com/>.

## TABLE OF CONTENTS (TOC)

Authors are required to submit a graphic entry for the Table of Contents (TOC) in conjunction with the manuscript title. This graphic should capture the readers' attention and give readers a visual impression of the essence of the paper. Labels, formulae, or numbers within the graphic must be legible at publication size. Tables or spectra are not acceptable. Color graphics are highly encouraged. The resolution of the figure should be at least 600 dpi. The size should be at least 50 mm × 80 mm with a rectangular shape (ideally, the ratio of height to width should be less than 1 and larger than 5/8). One to two sentences should be written below the figure to summarize the paper. To create the TOC, please insert your image in the template box below. Fonts, size, and spaces should not be changed.

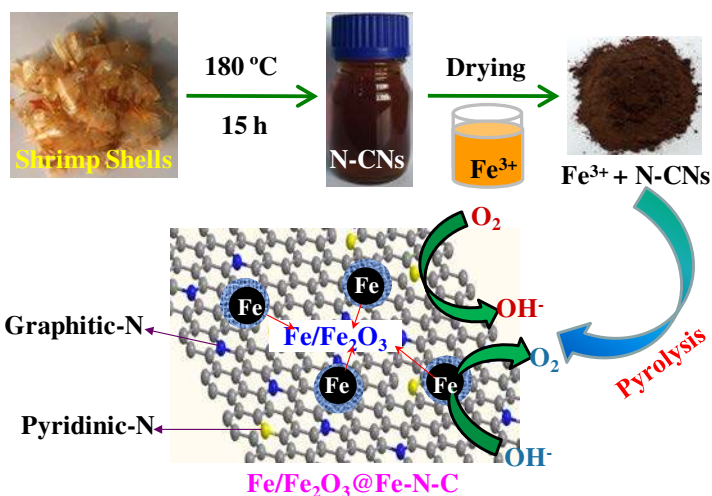
**Fe/Fe<sub>2</sub>O<sub>3</sub> nanoparticles anchored on Fe-N-doped carbon nanosheets as bifunctional oxygen electrocatalysts for rechargeable zinc-air batteries**

Yipeng Zang<sup>1,2</sup>, Haimin Zhang<sup>1,\*</sup>, Xian Zhang<sup>1,2</sup>, Rongrong Liu<sup>1,2</sup>, Shengwen Liu<sup>1</sup>, Guozhong Wang<sup>1</sup>, Yunxia Zhang<sup>1</sup> and Huijun Zhao<sup>1,3,\*</sup>

<sup>1</sup> Key Laboratory of Materials Physics, Centre for Environmental and Energy Nanomaterials, Anhui Key Laboratory of Nanomaterials and Nanotechnology, Institute of Solid State Physics, Chinese Academy of Sciences, Hefei 230031, China.

<sup>2</sup> University of Science and Technology of China, Hefei 230026, China.

<sup>3</sup> Centre for Clean Environment and Energy, Griffith University, Gold Coast Campus, QLD 4222, Australia.



Shrimp-shell derived N-doped carbon nanodots (N-CNs) were used as carbon and nitrogen sources to fabricate Fe/Fe<sub>2</sub>O<sub>3</sub> nanoparticles anchored on Fe-N-doped carbon nanosheets by a simple pyrolysis approach, as electrocatalysts exhibiting bifunctional catalytic activities toward oxygen reduction and evolution reactions and great potential as air cathode materials for rechargeable zinc-air batteries.

Provide the authors' website if possible. Author 1, website 1; Author 2, website 2



# Fe/Fe<sub>2</sub>O<sub>3</sub> nanoparticles anchored on Fe-N-doped carbon nanosheets as bifunctional oxygen electrocatalysts for rechargeable zinc-air batteries

Yipeng Zang<sup>1,2</sup>, Haimin Zhang<sup>1</sup>(✉), Xian Zhang<sup>1,2</sup>, Rongrong Liu<sup>1,2</sup>, Shengwen Liu<sup>1</sup>, Guozhong Wang<sup>1</sup>, Yunxia Zhang<sup>1</sup> and Huijun Zhao<sup>1,3</sup>(✉)

<sup>1</sup> Key Laboratory of Materials Physics, Centre for Environmental and Energy Nanomaterials, Anhui Key Laboratory of Nanomaterials and Nanotechnology, Institute of Solid State Physics, Chinese Academy of Sciences, Hefei 230031, China.

<sup>2</sup> University of Science and Technology of China, Hefei 230026, China.

<sup>3</sup> Centre for Clean Environment and Energy, Griffith University, Gold Coast Campus, QLD 4222, Australia.

Received: day month year

Revised: day month year

Accepted: day month year  
(automatically inserted by the publisher)

© Tsinghua University Press  
and Springer-Verlag Berlin  
Heidelberg 2014

## KEYWORDS

N-doped carbon nanodots;  
Fe/Fe<sub>2</sub>O<sub>3</sub>@Fe-N-doped  
carbon;  
oxygen reduction reaction;  
oxygen evolution reaction;  
rechargeable zinc-air  
battery

## ABSTRACT

Electrocatalysts with high catalytic activity and stability play key role in some promising renewable energy technologies, such as fuel cells and metal-air batteries. Here, we reported the synthesis of Fe/Fe<sub>2</sub>O<sub>3</sub> nanoparticles anchored on Fe-N-doped carbon nanosheets (Fe/Fe<sub>2</sub>O<sub>3</sub>@Fe-N-C) using shrimp-shell derived N-doped carbon nanodots as carbon and nitrogen sources in the presence of FeCl<sub>3</sub> by a simple pyrolysis approach. The results demonstrated that Fe/Fe<sub>2</sub>O<sub>3</sub>@Fe-N-C obtained at pyrolysis temperature of 1000 °C (Fe/Fe<sub>2</sub>O<sub>3</sub>@Fe-N-C-1000) possessed a mesoporous structure and high surface area of 747.3 m<sup>2</sup> g<sup>-1</sup>. As electrocatalyst, Fe/Fe<sub>2</sub>O<sub>3</sub>@Fe-N-C-1000 exhibited bifunctional electrocatalytic activities toward oxygen reduction reaction (ORR) and oxygen evolution reaction (OER) in alkaline media, comparable to that of commercial Pt/C for ORR and RuO<sub>2</sub> for OER, respectively. The test of zinc-air (Zn-air) battery demonstrated that Fe/Fe<sub>2</sub>O<sub>3</sub>@Fe-N-C-1000 as air cathode material showed superior rechargeable performance and cycling stability with an open circuit voltage of 1.47 V (*vs.* Ag/AgCl) and a power density of 193 mW cm<sup>-2</sup> at current density of 220 mA cm<sup>-2</sup>, better than commercial catalyst with an open circuit voltage of 1.36 V and a power density of 173 mW cm<sup>-2</sup> at current density of 220 mA cm<sup>-2</sup> (a mixture of commercial Pt/C and RuO<sub>2</sub> with a mass ratio of 1:1 was used for rechargeable Zn-air battery measurements). This work would be helpful to design and develop low-cost and abundant bifunctional oxygen electrocatalysts for future metal-air batteries.



## 1 Introduction

Rechargeable zinc-air (Zn-air) battery as renewable energy technology has recently attracted increasing research attention owing to its low cost, compact structure configuration and high power density [1-5]. For practical use of rechargeable Zn-air batteries, it is critically important to develop low-cost, abundant and high-performance electrocatalysts with superior catalytic activities toward both oxygen reduction reaction (ORR) and oxygen evolution reaction (OER) due to the batteries' performance directly related to the electrocatalysts' bifunctional ORR and OER catalytic activities [1-3, 6, 7]. To date, Pt-based materials have been proven to be the most efficient catalysts for ORR, but showing poor OER catalytic activity [8]; ruthenium/iridium oxides have been widely accepted as the most active catalysts for OER, while their ORR performance is very low [9]. These noble metal/metal oxide electrocatalysts with superior catalytic activity toward either ORR or OER cannot meet the requirements as bifunctional oxygen electrocatalysts in rechargeable Zn-air batteries [8-10]. More importantly, the high cost and source scarcity of these commercial ORR/OER electrocatalysts have been the biggest limitation for their scale-up applications [11, 12]. Therefore, it is highly desired for developing low-cost, abundant and high performance electrocatalysts with bifunctional catalytic activities toward both ORR and OER for rechargeable Zn-air batteries.

Recently, transition metal (*e.g.*, Fe, Co *etc.*) contained N-doped carbon materials have demonstrated great potential in primary Zn-air/rechargeable Zn-air batteries due to their intrinsically high electrocatalytic activities toward ORR or both ORR and OER [1-5, 13, 14]. For Fe active species contained N-doped carbon materials, such as Fe-N-doped carbon [15, 16], Fe nanoparticle@N-doped carbon [2, 17], iron

oxide@N-doped carbon [18], and iron carbide@N-doped carbon [4, 7, 19, 20], have been developed and investigated as electrocatalysts for ORR or both ORR and OER, exhibiting superior electrocatalytic activities. The theoretical and experimental results have revealed that various Fe active species incorporating N doping in carbon structures can effectively create catalytic active sites, combined with the advantageous characteristics of carbon structures such as high surface area and porous property, resulting in high ORR or bifunctional ORR and OER performance [2, 4, 17, 21]. However, most works on the aforementioned Fe active species contained N-doped carbon materials are almost used as only ORR or OER electrocatalysts for half-cell reaction study of a Zn-air battery [15, 18, 20, 22]. To date, only few reports have demonstrated that Fe active species contained N-doped carbon materials can be assembled into a real Zn-air battery for primary or rechargeable battery measurements, exhibiting high performance and cycling stability, but still far from practical applications [2-5, 23]. Therefore, exploring more Fe-based N-doped carbon materials with high bifunctional ORR and OER catalytic activities is still highly requested for meeting the practical needs of Zn-air batteries.

Generally, Fe active species contained N-doped carbon materials are fabricated by high temperature pyrolysis approach, for example, one-step synthesis in the presence of Fe, carbon and nitrogen precursors and two-step synthesis by post-treating N-doped carbon structures in the presence of Fe precursor [2, 4, 19, 20]. No matter what synthetic method is adopted, nitrogen and carbon contained chemicals are necessary during high temperature pyrolysis to obtain N-doped carbon structures in most studies [2, 4, 18, 19], undoubtedly improving the cost of practical applications. Recently, N-doped carbon materials derived from raw biomasses such as grass and shrimp shell *etc.* have demonstrated great potential as electrocatalysts for ORR [24-27]. Our

Address correspondence to Haimin Zhang, [zhanghm@issp.ac.cn](mailto:zhanghm@issp.ac.cn); Huijun Zhao, [h.zhao@griffith.edu.au](mailto:h.zhao@griffith.edu.au)

recent work also demonstrates shrimp-shell derived N-doped carbon nanodots can be used as carbon and nitrogen sources to further assemble and transform into three-dimensional N-doped porous graphitic carbon for high efficient ORR [27]. This inspired us to utilize such low-cost and abundant biomass-derived N-doped carbon nanodots as carbon and nitrogen sources to fabricate high performance non-precious metal contained N-doped carbon electrocatalysts with bifunctional ORR and OER activities for rechargeable Zn-air battery applications.

Herein, we reported the synthesis of  $\text{Fe}/\text{Fe}_2\text{O}_3$  nanoparticles anchored on Fe-N-doped carbon nanosheets ( $\text{Fe}/\text{Fe}_2\text{O}_3@\text{Fe-N-C}$ ) using shrimp-shell derived N-doped carbon nanodots as precursor in the presence of  $\text{FeCl}_3$  by a simple high temperature pyrolysis approach. The resulting  $\text{Fe}/\text{Fe}_2\text{O}_3@\text{Fe-N-C}$  composites were used as electrocatalysts to evaluate their electrocatalytic activities toward both ORR and OER. The experimental results indicated that  $\text{Fe}/\text{Fe}_2\text{O}_3@\text{Fe-N-C}$  obtained at pyrolysis temperature of 1000 °C ( $\text{Fe}/\text{Fe}_2\text{O}_3@\text{Fe-N-C-1000}$ ) exhibited superior ORR activity in both alkaline and acidic media, comparable to that of commercial Pt/C catalyst. Simultaneously, the  $\text{Fe}/\text{Fe}_2\text{O}_3@\text{Fe-N-C-1000}$  also showed high OER catalytic activity, comparable to that of commercial  $\text{RuO}_2$  catalyst. The  $\text{Fe}/\text{Fe}_2\text{O}_3@\text{Fe-N-C-1000}$  with bifunctional ORR and OER activities was used as air cathode material, manifesting high performance and cycling stability in a rechargeable Zn-air battery.

## 2 Experimental

### 2.1 Synthesis of N-doped carbon nanodots from shrimp shells

Shrimp-shell derived N-doped carbon nanodots (N-CNs) were synthesized using a similar method reported by us [27]. In a typical synthesis, the shrimp shells were first dried at 80 °C for 12 h, and then ground into powder as reaction precursor. Next, 10 g shrimp-shell powder was

added to 60 mL of deionized water, and then transferred into a 100 mL of Teflon-lined autoclave and kept at 180 °C for 15 h. After hydrothermal reaction, the obtained mixture was adequately filtrated to remove large size residues by simple filtration approach (two times using 0.45  $\mu\text{m}$  Millipore filter; one time using 0.22  $\mu\text{m}$  Millipore filter). The obtained solution was further treated by centrifugation at 14,000 rpm for 15 min to collect the supernate, and then the supernate was further dialyzed for two days to remove all kinds of inorganic ions for further characterization and use. The product yield of N-CNs is ~38.2% and the concentration of N-CNs solution is ~63.7 mg mL<sup>-1</sup>.

### 2.2 Synthesis of $\text{Fe}/\text{Fe}_2\text{O}_3@\text{Fe-N-C}$ composites

In a typical synthesis, 10 mL of 63.7 mg mL<sup>-1</sup> N-CNs and 10 mL of 40 mg mL<sup>-1</sup>  $\text{FeCl}_3$  solution were first mixed and then shocked with a speed of 200 rpm at 25 °C for 6 h in a shaking table. Subsequently, the above mixture was dried at 60 °C for overnight, and then pyrolytically treated at different pyrolysis temperatures (800 °C, 900 °C, 1000 °C and 1100 °C) in  $\text{N}_2$  atmosphere for 1 h. To remove the impurities, the pyrolytic products at different temperatures were immersed in 0.5 M  $\text{H}_2\text{SO}_4$  solution at 80 °C for 9 h under vigorously stirring, followed by filtration and washing with ethanol and deionized water. Finally, the acid-leaching products with different pyrolysis temperatures were again pyrolytically treated at the same temperatures as the aforementioned procedure at  $\text{N}_2$  atmosphere for 3 h to obtain  $\text{Fe}/\text{Fe}_2\text{O}_3$  nanoparticles anchored on Fe-N-doped carbon nanosheet composites ( $\text{Fe}/\text{Fe}_2\text{O}_3@\text{Fe-N-C-X}$ , X represents pyrolysis temperature of 800 °C, 900 °C, 1000 °C and 1100 °C).

### 2.3 Characterization

The crystalline structures of samples were identified by X-ray diffraction analysis (XRD, Philips X'pert PRO) using Nifiltered monochromatic Cu K $\alpha$  radiation ( $\lambda\text{K}\alpha_1 = 1.5418 \text{ \AA}$ ) at 40 kV and 40 mA. The morphology and structure of samples were



characterized by field emission scanning electron microscopy (FESEM, Quanta 200FEG) and transmission electron microscopy (TEM, JEOL 2010) with an energy dispersive X-ray spectrometer (EDS Oxford, Link ISIS). X-ray photoelectron spectroscopy (XPS) analysis was performed on an ESCALAB 250 X-ray photoelectron spectrometer (Thermo, America) equipped with Al K $\alpha$ 1, 2 monochromatized radiation at 1486.6 eV X-ray source. The surface area and porosity of samples were measured by a Surface Area and Porosity Analyzer (Tristar3020M). Raman patterns of the samples were measured in an Ar ion laser operating at 632 nm on a LabRAM HR800 confocal microscope Raman system (Horiba Jobin Yvon). **The thermogravimetric analysis of samples was performed on a Thermogravimetric Analyzer (SDT Q600 V20.9 Build 20, TA Instrument Inc., USA).**

#### 2.4 Electrochemical measurements

All ORR and OER tests were carried out on an electrochemical station (CHI 660E, CH Instrument, Inc., shanghai, China) combined with a PINE rotating disk electrode (RDE) system (Pine Instruments Co. Ltd. USA). A glassy carbon (GC) electrode (5.0 mm in diameter) served as the substrate of electrocatalyst was used as working electrode. Ag/AgCl and Pt wire were used as reference and counter electrodes, respectively. A conventional three-electrode electrochemical cell with a flowing gas system was applied for electrochemical measurements.

Prior to use, GC electrode was first polished with 5.0, 3.0 and 0.05  $\mu\text{m}$  alumina slurry sequentially and then washed ultrasonically in water and ethanol for 30 s, respectively. The cleaned electrode was then dried with a high-purify nitrogen steam. The **Fe/Fe<sub>2</sub>O<sub>3</sub>@Fe-N-C** catalyst ink was prepared by dispersing catalyst powder (10 mg) into a mixture including 100  $\mu\text{L}$  of Nafion solution (0.5 wt.%) and 900  $\mu\text{L}$  of ethanol, followed by ultrasonic treatment for 2 min. After that, 12  $\mu\text{L}$

of catalyst ink was then cast onto GC electrode surface. For comparison, **commercial E-TEK Pt/C (20 wt.%)** and **RuO<sub>2</sub> (Aldrich)** catalyst inks were also made as the same procedure as **Fe/Fe<sub>2</sub>O<sub>3</sub>@Fe-N-C** catalyst ink.

The ORR performance of **Fe/Fe<sub>2</sub>O<sub>3</sub>@Fe-N-C** electrocatalyst was measured by cyclic voltammogram (CV) in N<sub>2</sub>- and O<sub>2</sub>-saturated 0.1 M KOH solution and linear sweep voltammogram (LSV) in O<sub>2</sub>-saturated 0.1 M KOH solution. The CVs was tested from 0.2 V to -0.8 V with a scan rate of 50 mV s<sup>-1</sup> and LSVs was measured from 0.2 V to -0.8 V at a scan rate of 10 mV s<sup>-1</sup> with different disk rotation rates of 400, 625, 900, 1225, 1600 and 2025 rpm, respectively. The ORR performance of **Fe/Fe<sub>2</sub>O<sub>3</sub>@Fe-N-C** electrocatalyst was also evaluated in N<sub>2</sub>- and O<sub>2</sub>-saturated 0.1 M HClO<sub>4</sub> solution. The OER performance of **Fe/Fe<sub>2</sub>O<sub>3</sub>@Fe-N-C** electrocatalyst was performed in an O<sub>2</sub>-saturated 0.1 M KOH solution at a scan rate of 5.0 mV s<sup>-1</sup> under a rotation speed of 1600 rpm. The electron transfer number (*n*) per oxygen molecule in an ORR process was calculated by the Koutecky-Levich (K-L) equation [28, 29]:

$$J^{-1} = J_k^{-1} + (B\omega^{1/2})^{-1} \quad (1)$$

$$B = 0.62nF(D_0)^{2/3}\nu^{-1/6}C_0 \quad (2)$$

$$J_k = nFkC_0 \quad (3)$$

where *J* is the measured current density during ORR, *J<sub>k</sub>* is the kinetic current density,  $\omega$  is the electrode rotating angular velocity ( $\omega = 2\pi N$ , *N* is the linear rotation speed), *B* is the slope of K-L plots, *n* represents the electron transfer number per oxygen molecule, *F* is the Faraday constant ( $F = 96485 \text{ C mol}^{-1}$ ), *D<sub>0</sub>* is the diffusion coefficient of O<sub>2</sub> in 0.1 M KOH ( $1.9 \times 10^{-5} \text{ cm}^2 \text{ s}^{-1}$ ),  $\nu$  is the kinetic viscosity ( $0.01 \text{ cm}^2 \text{ s}^{-1}$ ), *C<sub>0</sub>* is the bulk concentration of O<sub>2</sub> ( $1.2 \times 10^{-3} \text{ mol L}^{-1}$ ). The ORR performance of catalysts was also evaluated in O<sub>2</sub> (or N<sub>2</sub>)-saturated 0.1 M HClO<sub>4</sub> solution with other test conditions kept the same. In 0.1 M HClO<sub>4</sub> solution, the diffusion coefficient *D<sub>0</sub>* is  $2.0 \times 10^{-5} \text{ cm}^2 \text{ s}^{-1}$ , and the

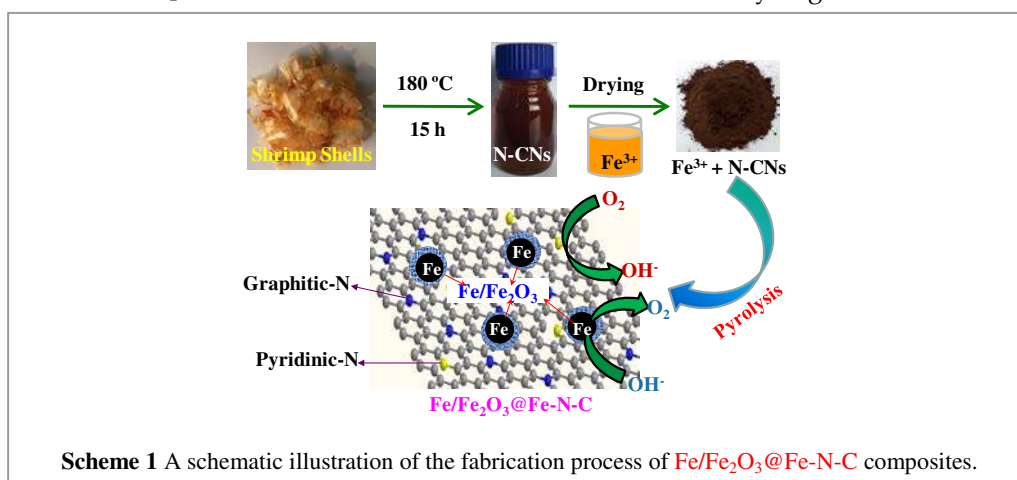
bulk concentration of  $O_2$  ( $C_0$ ) is  $1.5 \times 10^{-3} \text{ mol L}^{-1}$ .

The measurements of rechargeable zinc-air batteries were performed on home-built electrochemical cells [4]. All data were collected from the as-fabricated cell with a CHI 760D (CH Instruments, Inc., Shanghai, China) electrochemical workstation at room temperature. Briefly, zinc foil was used as anode and catalyst loaded on the gas diffusion layer (Teflon-coated carbon fiber paper with a geometric area of  $1.0 \text{ cm}^2$ , catalyst loading amount of  $2.0 \text{ mg cm}^{-2}$ ) was used as the air cathode. The electrolyte was  $6.0 \text{ M KOH}$  or  $6.0 \text{ M KOH} + 0.2 \text{ M}$  zinc acetate.

### 3 Results and discussion

Our previous work has demonstrated that shrimp-shell derived carbon nanodots (N-CNs) possess small nanodot sizes of  $1.5\text{--}5.0 \text{ nm}$  and rich surface O- and N-containing functional groups (e.g., O-H, N-H, C-N, C=O/C=N) [27]. These benefits enable N-CNs as carbon and nitrogen sources to fabricate non-precious metal contained N-doped carbon materials for electrocatalysis applications. Scheme 1 shows a schematic fabrication process of  $Fe/Fe_2O_3@Fe\text{-N-C}$  composites by a pyrolysis approach at different temperatures. Figure 1A shows the XRD patterns of  $Fe/Fe_2O_3@Fe\text{-N-C}$  composites at different pyrolysis temperatures. As shown, all pyrolytic samples exhibit inter-plane (002) diffraction

peaks at around  $24.7^\circ$ , attributed to graphitic carbon [30]. Additionally, the diffraction peaks of **metallic Fe** and  $Fe_2O_3$  can be also clearly observed in XRD patterns for all samples. Moreover, the intensities of diffraction peaks of  $Fe_2O_3$  obviously enhance with increasing pyrolysis temperature, indicating high pyrolysis temperature favourable for the formation of  $Fe_2O_3$ . The oxygen element in  $Fe_2O_3$  is believed to be mainly originated from the surface O-containing functional groups of N-CNs during high temperature pyrolysis [27]. Figure 1B shows the surface SEM image of pyrolytic sample (take  $Fe/Fe_2O_3@Fe\text{-N-C-1000}$  as an example). After pyrolysis treatment,  $Fe/Fe_2O_3@Fe\text{-N-C-1000}$  displays the morphology of aggregates. Further TEM analysis (Figure 1C) reveals that  $Fe/Fe_2O_3@Fe\text{-N-C-1000}$  is mainly composed of graphitic carbon nanosheets with uniformly distributed Fe-related nanoparticles with sizes of  $10\text{--}50 \text{ nm}$ . The HRTEM image (Figure 1D) of an individual Fe-related nanoparticle shows the lattice spacings of  $0.20 \text{ nm}$  and  $0.25 \text{ nm}$ , which are ascribed to the (011) and (311) planes of **metallic Fe** and  $\gamma\text{-}Fe_2O_3$ , respectively. **Obviously, the nanoparticle exhibits a structure of  $Fe/Fe_2O_3$  co-existence.** The energy-filtered TEM (EFTEM) imaging confirms the presence of C, O and Fe elements in  $Fe/Fe_2O_3@Fe\text{-N-C-1000}$  with homogeneously distributed characteristics (Figure S1 in the ESM). In this work, no N element was detected using EFTEM analysis possibly owing to low N doping content in  $Fe/Fe_2O_3@Fe\text{-N-C-1000}$ , however, N element may be detected by high resolution XPS technique.





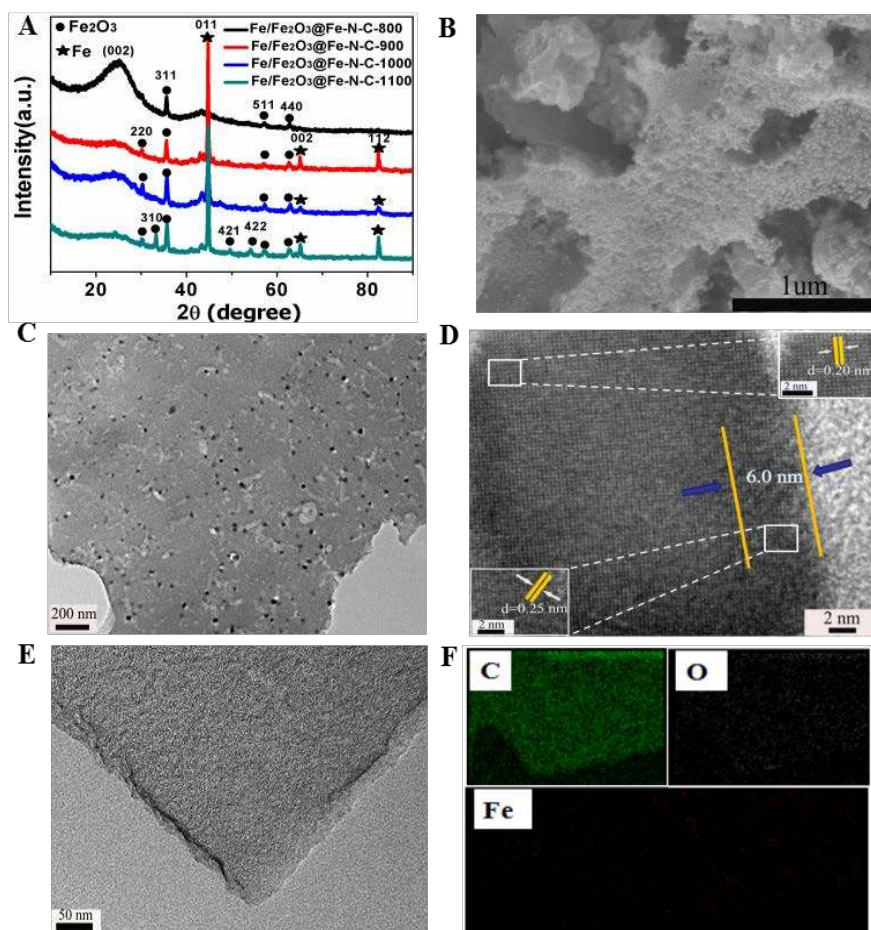


**Figure 1** (A) XRD patterns of  $\text{Fe}/\text{Fe}_2\text{O}_3@/\text{Fe-N-C}$  composites obtained at different pyrolysis temperatures. (B) Surface SEM image of  $\text{Fe}/\text{Fe}_2\text{O}_3@/\text{Fe-N-C-1000}$ . (C) TEM image of  $\text{Fe}/\text{Fe}_2\text{O}_3@/\text{Fe-N-C-1000}$ . (D) High resolution TEM image of an individual  $\text{Fe}/\text{Fe}_2\text{O}_3$  particle; the insets of high resolution TEM images of Fe and  $\text{Fe}_2\text{O}_3$ . (E) TEM image of an individual carbon nanosheet without  $\text{Fe}/\text{Fe}_2\text{O}_3$  particles. (F) EFTEM element mapping images of C, O and Fe of  $\text{Fe}/\text{Fe}_2\text{O}_3@/\text{Fe-N-C-1000}$  obtained from Figure 1E.

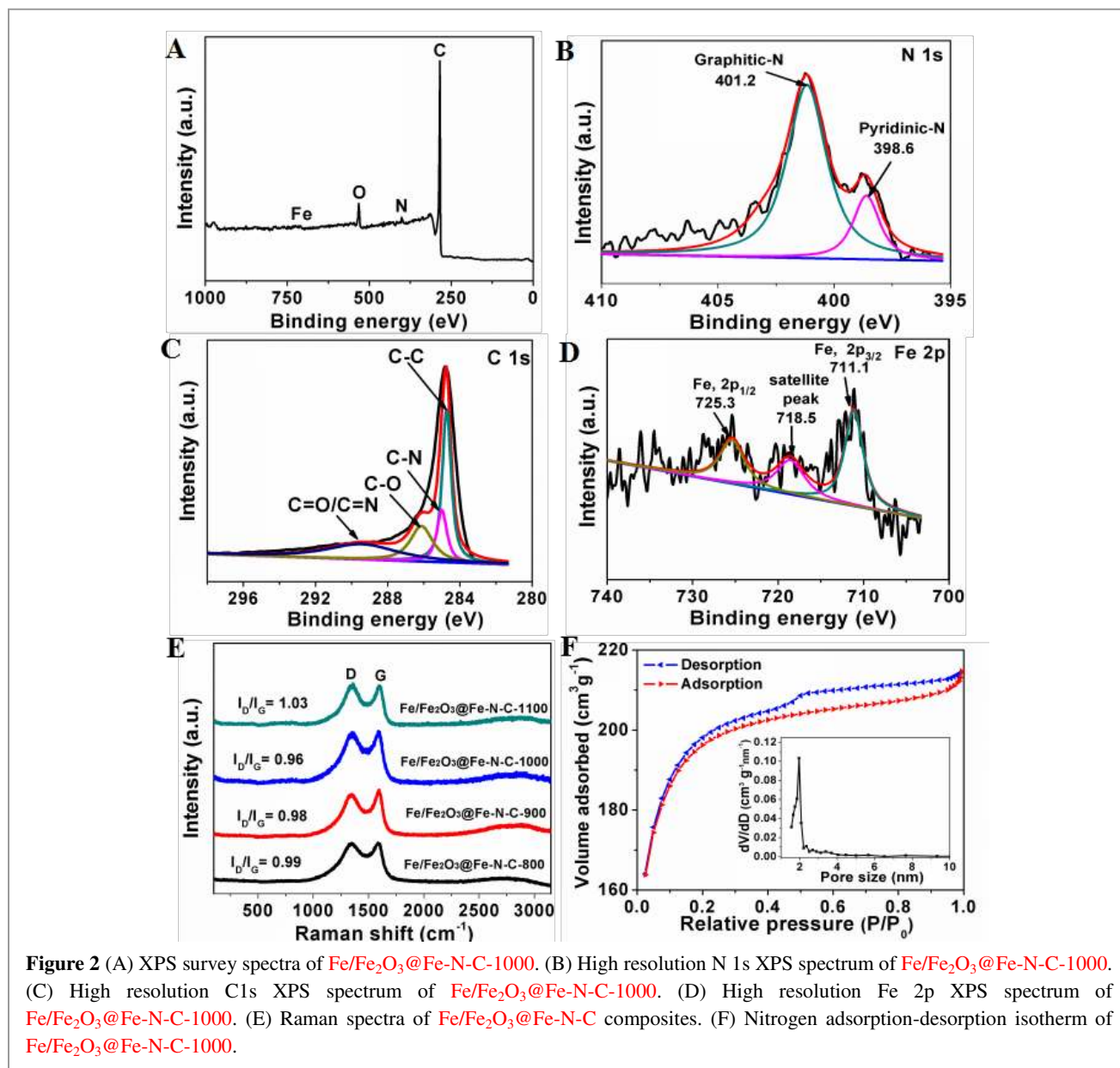
Interestingly, it is found that the area of carbon nanosheet without  $\text{Fe}/\text{Fe}_2\text{O}_3$  nanoparticles also exhibits the presence of C, O and Fe elements, implying Fe doping in graphitic carbon structure (Figure 1E, F). Energy dispersive X-ray diffraction spectroscopy (EDS) indicates that Fe doping content is  $\sim 0.13$  at.% in graphitic carbon nanosheet (Figure S2A in the ESM). Figure S2B, C (in the ESM) show the TG/DSC curves of  $\text{Fe}^{3+}$  contained N-CN sample conducted in air and  $\text{N}_2$  atmospheres from room temperature to 1000 °C. As shown in air atmosphere (Figure S2B in the ESM), two weight losses were observed from room temperature to 1000 °C owing to the evaporation of water physically adsorbed on the sample (weight loss of 4.3 wt.% at the

temperature range of room temperature to 150 °C) and the decomposition of N-doped carbon nanodots to form  $\text{CO}_2$  (weight loss of 74.8 wt.% from 368 °C to 608 °C). Finally, a stable status was achieved from 608 °C to 1000 °C due to the formation of stable iron oxide (e.g.,  $\text{Fe}_3\text{O}_4$ , 20.9 wt.%). In  $\text{N}_2$  atmosphere, the TG/DSC curves of sample are very different with those obtained in air. As shown in Figure S2C (in the ESM), three weight losses were observed from room temperature to 1000 °C ascribed to the evaporation of physically adsorbed water (weight loss of 10.3 wt.% from room temperature to 150 °C), the semi-carbonization of N-CN (weight loss of 0.95 wt.% from 150 °C to 346 °C), and the transformation of graphitic carbon (weight loss of

17.1 wt.% from 504 °C to 1000 °C). The weight percentage of the formed Fe/Fe<sub>2</sub>O<sub>3</sub>@graphitic carbon is about 71.7 wt.%. In N<sub>2</sub> atmosphere, the TG curve of sample is still decreased from 504 °C to 1000 °C, possibly attributed to graphitic carbon loss resulting from the presence of remnant oxygen to form carbon oxide with temperature.

Further, XPS technique was employed to analyze the element composition of Fe/Fe<sub>2</sub>O<sub>3</sub>@Fe-N-C-1000. The surface survey XPS spectra show the presence of C (89.8%), N (3.1%), O (6.8%) and Fe (0.3%) elements in sample (Figure 2A). The high resolution N 1s XPS spectrum (Figure 2B) can be divided into two peaks at 398.6 eV and 401.2 eV, corresponding to pyridinic-N (18.5%) and graphitic-N (81.5%), implying high pyrolysis temperature favourable for the transformation of pyrrolic-N into graphitic-N [4, 25, 30, 31]. Many studies have addressed that pyridinic-N and graphitic-N in carbon structure are very beneficial N doping forms to create catalytic active sites for electrocatalysis [4, 25, 30, 31]. In addition, some studies have indicated that the peak at a binding energy of 398.6 eV may include a contribution from nitrogen bound to iron (Fe-N) due to a very small difference between binding energies of pyridinic-N and Fe-N [4, 32]. The high resolution C 1s spectrum (Figure 2C) can be divided into four peaks at around 284.7 eV, 285.1 eV, 286.2 eV and 289.7 eV, assigned to C-C, C-N, C-O and C=O/C=N, respectively [4, 25, 27]. The above results further confirm N doping and surface O- and N-containing functional groups in Fe/Fe<sub>2</sub>O<sub>3</sub>@Fe-N-C-1000. Figure 2D shows high resolution Fe 2p XPS spectrum. As shown, the Fe 2p spectrum can be deconvoluted into three peaks, and the bonding energies at around 711.1 eV and 725.3 eV can be due to the binding energies of the 2p<sub>3/2</sub> and 2p<sub>1/2</sub> bands of Fe<sup>3+</sup>, respectively, originated from Fe<sub>2</sub>O<sub>3</sub> in Fe/Fe<sub>2</sub>O<sub>3</sub>@Fe-N-C-1000 [4, 15, 33]. The bonding energy at 718.5 eV can be ascribed to a satellite peak [4, 15]. Additionally, the peak at 711.1 eV in the Fe 2p<sub>3/2</sub> XPS spectrum also indicates that Fe

ions may coordinate to N to form Fe-N bonding [4, 34]. The above results combined with electron microscopy analysis confirm the formation of Fe/Fe<sub>2</sub>O<sub>3</sub> co-existed nanoparticles anchored on Fe-N-doped carbon nanosheets. Figure 2E shows the Raman spectra of Fe/Fe<sub>2</sub>O<sub>3</sub>@Fe-N-C composites obtained at different pyrolysis temperatures. As shown, all samples exhibit two conspicuous diffraction peaks at near 1580 cm<sup>-1</sup> of the G band and 1352 cm<sup>-1</sup> of the D band, corresponding to the E<sub>2g</sub> vibration of the sp<sup>2</sup>-bonded carbon atoms and the disordered graphitic carbon [35]. The I<sub>D</sub>/I<sub>G</sub> values shown in Figure 2E are 0.99, 0.98, 0.96 and 1.03 for Fe/Fe<sub>2</sub>O<sub>3</sub>@Fe-N-C-800, Fe/Fe<sub>2</sub>O<sub>3</sub>@Fe-N-C-900, Fe/Fe<sub>2</sub>O<sub>3</sub>@Fe-N-C-1000 and Fe/Fe<sub>2</sub>O<sub>3</sub>@Fe-N-C-1100, respectively, indicating that disordered carbon first decreases with pyrolysis temperature, then increases at higher pyrolysis temperature of 1100 °C. With increasing pyrolysis temperature, the decrease in disordered carbon implies an increase of graphitization degree of carbon structure, favourable for electron transfer for electrocatalysis, while too high pyrolysis temperature (*e.g.*, 1100 °C) may arouse the structural damage of graphitic carbon, resulting in an increase of disordered carbon possibly unfavorable for electron transfer. In this work, Fe/Fe<sub>2</sub>O<sub>3</sub>@Fe-N-C-1000 shows the lowest I<sub>D</sub>/I<sub>G</sub> value among all samples investigated, indicating a high graphitization degree beneficial for electrocatalysis application. Figure 2F shows the N<sub>2</sub> adsorption and desorption isotherm of Fe/Fe<sub>2</sub>O<sub>3</sub>@Fe-N-C-1000. It can be seen that Fe/Fe<sub>2</sub>O<sub>3</sub>@Fe-N-C-1000 possesses an approximate mesoporous structure with pore size distribution centered at ~1.95 nm and ~3.4 nm (Figure 2F and inset). The surface area and total pore volume are measured to be 747.3 m<sup>2</sup> g<sup>-1</sup> and 0.026 cm<sup>3</sup> g<sup>-1</sup>, which are favourable for the exposure of catalytic active sites and ORR/OER-related mass transport, thus improving electrocatalytic performance [4, 15]. Also, the surface areas and total pore volumes are 640.7 m<sup>2</sup> g<sup>-1</sup> and 0.020 cm<sup>3</sup> g<sup>-1</sup>, 689.4 m<sup>2</sup> g<sup>-1</sup> and 0.023 cm<sup>3</sup> g<sup>-1</sup>, and 791.1 m<sup>2</sup> g<sup>-1</sup> and 0.086



$\text{cm}^3 \text{g}^{-1}$  for  $\text{Fe}/\text{Fe}_2\text{O}_3@/\text{Fe-N-C-800}$ ,  $\text{Fe}/\text{Fe}_2\text{O}_3@/\text{Fe-N-C-900}$ , and  $\text{Fe}/\text{Fe}_2\text{O}_3@/\text{Fe-N-C-1100}$ , respectively, exhibiting approximate mesoporous structures (Figure S3 and Table S1 in the ESM). With increasing pyrolysis temperature, the increase of surface area and total pore volume of sample can be achieved, favourable for improving electrocatalytic performance. However, too high pyrolysis temperature (e.g., for  $\text{Fe}/\text{Fe}_2\text{O}_3@/\text{Fe-N-C-1100}$ ) may result in the structural damage and the increase of disordered carbon of material, unfavorable for high

efficiency electron transport in electrocatalysis application.

As electrocatalysts, the fabricated  $\text{Fe}/\text{Fe}_2\text{O}_3@/\text{Fe-N-C}$  composites obtained at different pyrolysis temperatures were evaluated for ORR and OER applications. First, we performed ORR measurements using  $\text{Fe}/\text{Fe}_2\text{O}_3@/\text{Fe-N-C}$  composites as electrocatalysts. The cyclic voltammogram (CV) measurements (Figure 3A) indicated that no cathodic reduction current peaks were observed for all  $\text{Fe}/\text{Fe}_2\text{O}_3@/\text{Fe-N-C}$  catalysts and commercial Pt/C catalyst in  $\text{N}_2$ -saturated 0.1 M KOH solution.



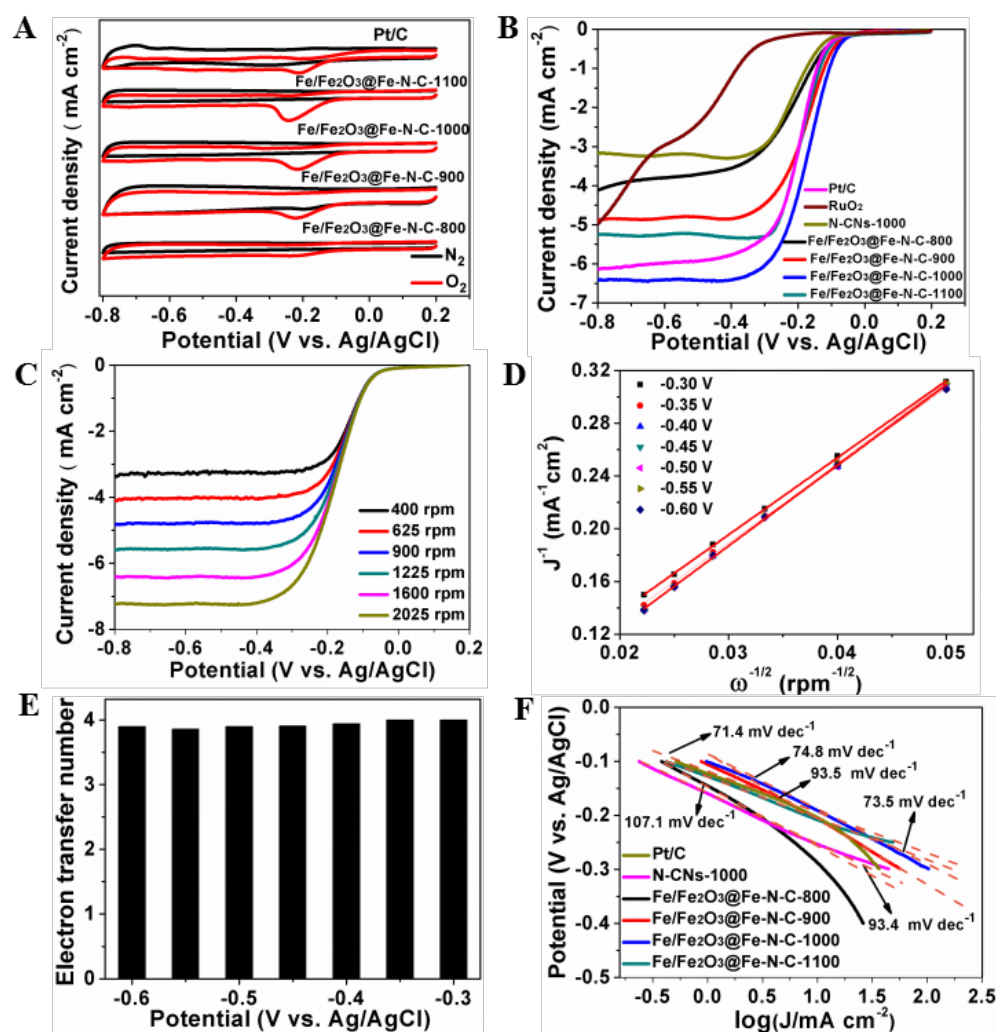


**Figure 3** (A) CV curves of all  $\text{Fe}/\text{Fe}_2\text{O}_3@/\text{Fe-N-C}$  electrocatalysts and Pt/C catalyst in  $\text{N}_2$ - or  $\text{O}_2$ -saturated 0.1 M KOH solution at a scan rate of  $50 \text{ mV s}^{-1}$ . (B) LSV curves of all  $\text{Fe}/\text{Fe}_2\text{O}_3@/\text{Fe-N-C}$  electrocatalysts, Pt/C,  $\text{RuO}_2$  and N-CNs-1000 at a scan rate of  $10 \text{ mV s}^{-1}$  with a rotation speed of 1600 rpm. (C) LSV plots of  $\text{Fe}/\text{Fe}_2\text{O}_3@/\text{Fe-N-C-1000}$  in  $\text{O}_2$ -saturated 0.1 M KOH solution at a scan rate of  $10 \text{ mV s}^{-1}$  with different rotation speeds. (D) K-L plots of  $\text{Fe}/\text{Fe}_2\text{O}_3@/\text{Fe-N-C-1000}$  obtained from Figure 3C at different potentials. (E) Electron transfer number ( $n$ ) of  $\text{Fe}/\text{Fe}_2\text{O}_3@/\text{Fe-N-C-1000}$  calculated from Figure 3D. (F) Tafel plots of all  $\text{Fe}/\text{Fe}_2\text{O}_3@/\text{Fe-N-C}$ , Pt/C and N-CNs-1000 electrocatalysts.

However, the cathodic reduction current peaks were found to be  $-0.228 \text{ V}$ ,  $-0.219 \text{ V}$ ,  $-0.210 \text{ V}$ ,  $-0.242 \text{ V}$ , and  $-0.208 \text{ V}$  in  $\text{O}_2$ -saturated 0.1 M KOH solution for  $\text{Fe}/\text{Fe}_2\text{O}_3@/\text{Fe-N-C-800}$ ,  $\text{Fe}/\text{Fe}_2\text{O}_3@/\text{Fe-N-C-900}$ ,  $\text{Fe}/\text{Fe}_2\text{O}_3@/\text{Fe-N-C-1000}$ ,  $\text{Fe}/\text{Fe}_2\text{O}_3@/\text{Fe-N-C-1100}$  and Pt/C catalysts, respectively. Apparently,  $\text{Fe}/\text{Fe}_2\text{O}_3@/\text{Fe-N-C-1000}$  possesses very close cathodic reduction peak potential ( $-0.210 \text{ V}$ ) to that ( $-0.208 \text{ V}$ ) of commercial Pt/C, indicating high ORR catalytic activity. Figure 3B shows the linear sweep voltammogram (LSV) curves of  $\text{Fe}/\text{Fe}_2\text{O}_3@/\text{Fe-N-C}$

catalysts in an  $\text{O}_2$ -saturated 0.1 M KOH solution under a rotation rate of 1600 rpm. For comparison, commercial Pt/C,  $\text{RuO}_2$  and N-CNs without  $\text{FeCl}_3$  precursor pyrolytically converted carbon material obtained at  $1000 \text{ }^\circ\text{C}$  (N-CNs-1000) were also used as electrocatalysts for ORR evaluation. As shown in Figure 3B, commercial  $\text{RuO}_2$  exhibits very poor ORR performance with an onset potential of  $-0.32 \text{ V}$ , whereas the onset potentials are  $-0.08 \text{ V}$ ,  $-0.06 \text{ V}$ ,  $-0.04 \text{ V}$ ,  $-0.07 \text{ V}$ ,  $-0.07 \text{ V}$  and  $-0.09 \text{ V}$  for  $\text{Fe}/\text{Fe}_2\text{O}_3@/\text{Fe-N-C-800}$ ,  $\text{Fe}/\text{Fe}_2\text{O}_3@/\text{Fe-N-C-900}$ ,  $\text{Fe}/\text{Fe}_2\text{O}_3@/\text{Fe-N-C-1000}$ ,

Fe/Fe<sub>2</sub>O<sub>3</sub>@Fe-N-C-1100, Pt/C and N-CNs-1000, respectively. Obviously, the Fe/Fe<sub>2</sub>O<sub>3</sub>@Fe-N-C-1000 shows smaller onset potential value than that of commercial Pt/C, indicating its highly intrinsic ORR catalytic activity. Further, the obtained half-wave potentials are -0.21 V, -0.19 V, -0.17 V, -0.19 V, -0.18 V and -0.22 V for Fe/Fe<sub>2</sub>O<sub>3</sub>@Fe-N-C-800, Fe/Fe<sub>2</sub>O<sub>3</sub>@Fe-N-C-900, Fe/Fe<sub>2</sub>O<sub>3</sub>@Fe-N-C-1000, Fe/Fe<sub>2</sub>O<sub>3</sub>@Fe-N-C-1100, Pt/C and N-CNs-1000, respectively. An approximate half-wave potential value of Fe/Fe<sub>2</sub>O<sub>3</sub>@Fe-N-C-1000 and commercial Pt/C further verifies high ORR catalytic activity of Fe/Fe<sub>2</sub>O<sub>3</sub>@Fe-N-C-1000. Compared to N-CNs-1000, Fe species incorporating in carbon structure apparently enhances the intrinsic ORR activity of catalyst. Moreover, a suitable pyrolysis temperature is critically important to obtain electrocatalyst with highly intrinsic ORR catalytic activity possibly owing to the formation of active species with apt content and type to create more catalytic active sites at such temperature. It can be also seen from Figure 3B, the Fe/Fe<sub>2</sub>O<sub>3</sub>@Fe-N-C-1000 exhibits larger limiting current density from -0.3 V to -0.8 V than that of other catalysts investigated, indicating its highly kinetic catalytic property of ORR. The superior ORR catalytic performance of Fe/Fe<sub>2</sub>O<sub>3</sub>@Fe-N-C-1000 may be due to a synergistic effect of Fe/Fe<sub>2</sub>O<sub>3</sub> nanoparticles and Fe, N doping in graphitic carbon structure combining with material's structure properties (e.g., high surface area and porous structure) to create more catalytic active sites and efficiently utilize these catalytic active sites [2, 4, 21, 22, 25, 28, 39]. With increasing pyrolysis temperature, the surface area/pore volume and graphitization degree (Figure 2E, F and Figure S3 in the ESM) of Fe/Fe<sub>2</sub>O<sub>3</sub>@Fe-N-C samples increase, favourable for the exposure of catalytic active sites, mass transport and electron transfer, thus improving ORR performance. However, too high pyrolysis temperature (e.g., 1100 °C) easily causes the increase of disordered carbon in graphitic carbon (Figure 2E) of the sample, which is disadvantageous for electron transfer in

electrocatalysis application, resulting in decreased ORR performance. Figure 3C shows the LSV responses of Fe/Fe<sub>2</sub>O<sub>3</sub>@Fe-N-C-1000 obtained from an O<sub>2</sub>-saturated 0.1 M KOH solution under different rotation rates. The cathodic current obviously enhances with increasing rotation rate, suggesting a mass transfer controlled process [36]. Further, the Koutecky-Levich (K-L) plots for Fe/Fe<sub>2</sub>O<sub>3</sub>@Fe-N-C-1000 derived from Figure 3C show good linear relationships, implying first-order reaction kinetics with regard to the concentration of dissolved oxygen and similar transferred electron numbers at different potentials (Figure 3D). The transferred electron numbers (*n*) are calculated to be from 3.85 to 4.0 at the potential range of -0.6 V to -0.3 V, suggesting a four-electron ORR process of Fe/Fe<sub>2</sub>O<sub>3</sub>@Fe-N-C-1000 (Figure 3E). Figure 3F shows the Tafel plots of different catalysts, exhibiting Tafel slopes of 107.1, 93.5, 74.8, 73.5, 71.4 and 93.4 mV dec<sup>-1</sup> for Fe/Fe<sub>2</sub>O<sub>3</sub>@Fe-N-C-800, Fe/Fe<sub>2</sub>O<sub>3</sub>@Fe-N-C-900, Fe/Fe<sub>2</sub>O<sub>3</sub>@Fe-N-C-1000, Fe/Fe<sub>2</sub>O<sub>3</sub>@Fe-N-C-1100, Pt/C and N-CNs-1000, respectively. Apparently, the Fe/Fe<sub>2</sub>O<sub>3</sub>@Fe-N-C-1000 possesses very close Tafel slope value to that of commercial Pt/C, further demonstrating its superior kinetic process of ORR [37]. The stability tests in O<sub>2</sub>-saturated 0.1 M KOH solution demonstrate that Fe/Fe<sub>2</sub>O<sub>3</sub>@Fe-N-C-1000 possesses very good durability with only 6.23% decrease in current density after 20,000 s of continuous run at a rotation rate of 1600 rpm, while Pt/C catalyst exhibits near 19% decrease in current density under the same experimental conditions (Figure S4A in the ESM). The crossover effect of small fuel molecule (e.g., methanol) on catalyst performance was also investigated in this work. The measurements of catalyst tolerance to methanol (Figure S4B in the ESM) demonstrate that Fe/Fe<sub>2</sub>O<sub>3</sub>@Fe-N-C-1000 exhibits high stability when 3.0 M methanol introduced into 0.1 M KOH solution, while commercial Pt/C shows a sharply decreased current under the same experimental conditions. The above results indicate

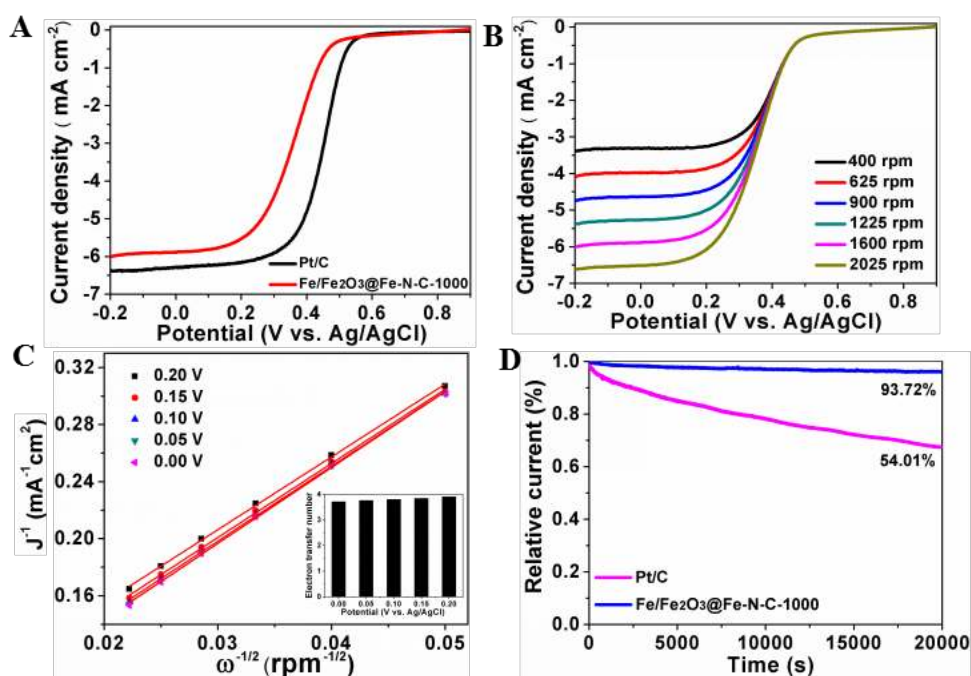


**Figure 4** (A) LSV plots of  $\text{Fe}/\text{Fe}_2\text{O}_3@/\text{Fe-N-C-1000}$  and commercial Pt/C catalysts in  $\text{O}_2$ -saturated 0.1 M  $\text{HClO}_4$  solution at the scan rate of  $10 \text{ mV s}^{-1}$  with a rotation speed of 1600 rpm. (B) LSV plots of  $\text{Fe}/\text{Fe}_2\text{O}_3@/\text{Fe-N-C-1000}$  in  $\text{O}_2$ -saturated 0.1 M  $\text{HClO}_4$  solution at the scan rate of  $10 \text{ mV s}^{-1}$  with different rotation speeds. (C) K-L plots of  $\text{Fe}/\text{Fe}_2\text{O}_3@/\text{Fe-N-C-1000}$  obtained from Figure 4B at different potentials and electron transfer number ( $n$ ) of  $\text{Fe}/\text{Fe}_2\text{O}_3@/\text{Fe-N-C-1000}$  calculated from Figure 4C (inset). (D) Durability tests of  $\text{Fe}/\text{Fe}_2\text{O}_3@/\text{Fe-N-C-1000}$  and commercial Pt/C catalysts at an applied potential of 0.20 V with a rotation speed of 1600 rpm.

$\text{Fe}/\text{Fe}_2\text{O}_3@/\text{Fe-N-C-1000}$  possessing high resistance to methanol crossover effect.

In this work, the ORR activity of  $\text{Fe}/\text{Fe}_2\text{O}_3@/\text{Fe-N-C-1000}$  was also evaluated in acidic media. Figure 4A shows the LSV curves of  $\text{Fe}/\text{Fe}_2\text{O}_3@/\text{Fe-N-C-1000}$  and commercial Pt/C catalysts in an  $\text{O}_2$ -saturated 0.1 M  $\text{HClO}_4$  solution under a rotation rate of 1600 rpm. As shown, the onset potential of  $\text{Fe}/\text{Fe}_2\text{O}_3@/\text{Fe-N-C-1000}$  is 0.52 V, close to that (0.58 V) of commercial Pt/C, indicating a good ORR catalytic activity of  $\text{Fe}/\text{Fe}_2\text{O}_3@/\text{Fe-N-C-1000}$  in acidic media. The K-L plots (Figure 4C) for  $\text{Fe}/\text{Fe}_2\text{O}_3@/\text{Fe-N-C-1000}$  derived from Figure 4B also exhibit good linear relationships, suggesting a first-order reaction toward the dissolved  $\text{O}_2$ . Based on Figure 4C, the transferred electron numbers ( $n$ ) were calculated to be 3.7–3.9 at the potential range of 0–0.20 V (inset in Figure 4C), implying a four-electron ORR process. The stability measurements in acid environment (Figure 4D) shows that

$\text{Fe}/\text{Fe}_2\text{O}_3@/\text{Fe-N-C-1000}$  has a good durability with only 6.28% decrease in current density after 20,000 s of continuous run at a rotation rate of 1600 rpm, whereas commercial Pt/C catalyst displays near 50% decrease in current density at the same process, indicating high stability of  $\text{Fe}/\text{Fe}_2\text{O}_3@/\text{Fe-N-C-1000}$  in acidic media. In a word, the  $\text{Fe}/\text{Fe}_2\text{O}_3@/\text{Fe-N-C-1000}$  possesses high ORR catalytic activity and durability in both alkaline and acidic conditions, which is very important for an ORR electrocatalyst for practical application.

As air cathode material, an electrocatalyst with bifunctional ORR and OER activities is necessary for a rechargeable Zn-air battery [1, 2]. In this work, the OER catalytic activity of  $\text{Fe}/\text{Fe}_2\text{O}_3@/\text{Fe-N-C}$ , commercial Pt/C and  $\text{RuO}_2$  catalysts was therefore evaluated in alkaline media using a three-electrode system. Figure 5A shows the polarization curves of all investigated catalysts. As shown,  $\text{Fe}/\text{Fe}_2\text{O}_3@/\text{Fe-N-C-1000}$  in 0.1



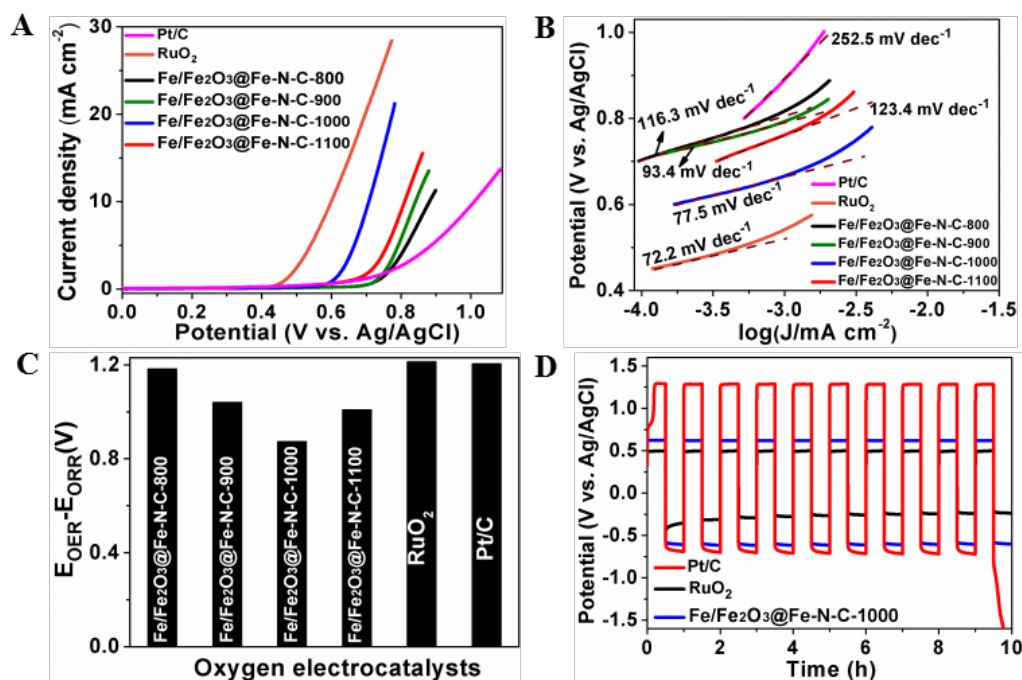


**Figure 5** (A) OER activity measurements of all  $\text{Fe}/\text{Fe}_2\text{O}_3@/\text{Fe-N-C}$  electrocatalysts, Pt/C and  $\text{RuO}_2$  at a scan rate of  $5.0 \text{ mV s}^{-1}$  with a rotation speed of 1600 rpm and the iR loss from the solution resistance was corrected. (B) Tafel curves of  $\text{Fe}/\text{Fe}_2\text{O}_3@/\text{Fe-N-C}$ , Pt/C and  $\text{RuO}_2$  catalysts. (C) The difference in potential between OER current density at  $10 \text{ mA cm}^{-2}$  and ORR current density at  $3.0 \text{ mA cm}^{-2}$  of all  $\text{Fe}/\text{Fe}_2\text{O}_3@/\text{Fe-N-C}$  electrocatalysts, Pt/C and  $\text{RuO}_2$  calculated from Figure 5A and Figure 3B. (D) Cycling durability of  $\text{Fe}/\text{Fe}_2\text{O}_3@/\text{Fe-N-C-1000}$ , Pt/C and  $\text{RuO}_2$  at  $1.0 \text{ mA cm}^{-2}$  with a rotation speed of 1600 rpm in a half cell.

M KOH electrolyte exhibits much higher OER current density than that of other  $\text{Fe}/\text{Fe}_2\text{O}_3@/\text{Fe-N-C}$  catalysts and Pt/C catalyst, comparable to that of commercial  $\text{RuO}_2$  catalyst, indicating a good OER performance of  $\text{Fe}/\text{Fe}_2\text{O}_3@/\text{Fe-N-C-1000}$ . It has been accepted that the potential required to oxidize water at the current density of  $10 \text{ mA cm}^{-2}$  is generally utilized to evaluate the OER activity of an electrocatalyst [2]. As shown in Figure 5A, the potentials at the current density of  $10 \text{ mA cm}^{-2}$  are 0.88 V, 0.84 V, 0.69 V, 0.80 V, 1.01 V and 0.59 V for  $\text{Fe}/\text{Fe}_2\text{O}_3@/\text{Fe-N-C-800}$ ,  $\text{Fe}/\text{Fe}_2\text{O}_3@/\text{Fe-N-C-900}$ ,  $\text{Fe}/\text{Fe}_2\text{O}_3@/\text{Fe-N-C-1000}$ ,  $\text{Fe}/\text{Fe}_2\text{O}_3@/\text{Fe-N-C-1100}$ , Pt/C and  $\text{RuO}_2$  catalysts, respectively. In comparison with other  $\text{Fe}/\text{Fe}_2\text{O}_3@/\text{Fe-N-C}$  catalysts and commercial Pt/C catalyst, the  $\text{Fe}/\text{Fe}_2\text{O}_3@/\text{Fe-N-C-1000}$  demonstrates smaller potential value at a current density of  $10 \text{ mA cm}^{-2}$ , close to that of commercial  $\text{RuO}_2$ , confirming good OER catalytic activity. Figure 5B shows the Tafel curves of  $\text{Fe}/\text{Fe}_2\text{O}_3@/\text{Fe-N-C}$ , commercial

Pt/C and  $\text{RuO}_2$  catalysts. The obtained Tafel slopes are 116.3, 93.4, 77.5, 123.4, 252.5 and  $72.2 \text{ mV dec}^{-1}$  for  $\text{Fe}/\text{Fe}_2\text{O}_3@/\text{Fe-N-C-800}$ ,  $\text{Fe}/\text{Fe}_2\text{O}_3@/\text{Fe-N-C-900}$ ,  $\text{Fe}/\text{Fe}_2\text{O}_3@/\text{Fe-N-C-1000}$ ,  $\text{Fe}/\text{Fe}_2\text{O}_3@/\text{Fe-N-C-1100}$ , Pt/C and  $\text{RuO}_2$  catalysts, respectively. Obviously, the Tafel slope ( $77.5 \text{ mV dec}^{-1}$ ) of  $\text{Fe}/\text{Fe}_2\text{O}_3@/\text{Fe-N-C-1000}$  is much smaller than that of other  $\text{Fe}/\text{Fe}_2\text{O}_3@/\text{Fe-N-C}$  and Pt/C catalysts, comparable to that ( $72.2 \text{ mV dec}^{-1}$ ) of commercial  $\text{RuO}_2$  catalyst, further indicating its high OER catalytic activity. Similar with ORR catalytic activity discussed, the high OER performance of  $\text{Fe}/\text{Fe}_2\text{O}_3@/\text{Fe-N-C-1000}$  may be due to  $\text{Fe}/\text{Fe}_2\text{O}_3$  nanoparticles and Fe, N-doping in graphitic carbon synergistically creating catalytic active sites and advantageous structural characteristics (e.g., high surface area, porous structure and high graphitization degree) efficiently utilizing these catalytic active sites [2, 4, 21, 22, 25, 28, 39]. In a word, the above results demonstrate that  $\text{Fe}/\text{Fe}_2\text{O}_3@/\text{Fe-N-C-1000}$  possesses bifunctional catalytic activities toward

both ORR and OER, enabling it as air cathode material for rechargeable Zn-air battery application. To further evaluate the bifunctional ORR and OER activities, the difference in potential ( $\Delta E$ ) between ORR current density at 3.0 mA cm<sup>-2</sup> and OER current density at 10 mA cm<sup>-2</sup> is adopted to reflect the bifunctionality of Fe/Fe<sub>2</sub>O<sub>3</sub>@Fe-N-C-1000 [2, 38]. The obtained  $\Delta E$  values (Figure 5C) are 1.18 V, 1.04 V, 0.87 V, 1.01 V, 1.22 V and 1.21 V for Fe/Fe<sub>2</sub>O<sub>3</sub>@Fe-N-C-800, Fe/Fe<sub>2</sub>O<sub>3</sub>@Fe-N-C-900, Fe/Fe<sub>2</sub>O<sub>3</sub>@Fe-N-C-1000, Fe/Fe<sub>2</sub>O<sub>3</sub>@Fe-N-C-1100, RuO<sub>2</sub> and Pt/C catalysts, respectively. It has been widely accepted that a low  $\Delta E$  value of an electrocatalyst indicates its high bifunctional catalytic activities toward both ORR and OER [2, 38]. By comparison, the Fe/Fe<sub>2</sub>O<sub>3</sub>@Fe-N-C-1000 exhibits the smallest  $\Delta E$  value among all catalysts investigated, confirming its highly intrinsic bifunctionality of ORR and OER. The cycling stability measurements (Figure 5D) show that Fe/Fe<sub>2</sub>O<sub>3</sub>@Fe-N-C-1000 possesses high durability in both ORR and OER processes under given

experimental conditions, which is critically important for a practical application in rechargeable Zn-air battery.

Recently, Fe-based N-doped carbon materials with ORR activity or both ORR and OER activities have demonstrated great potential as air cathode materials for primary and rechargeable Zn-air batteries [2-4, 23]. In this work, the primary and rechargeable Zn-air batteries were also measured using Fe/Fe<sub>2</sub>O<sub>3</sub>@Fe-N-C-1000 as air cathode material. For a meaningful comparison, a mixture of commercial Pt/C and RuO<sub>2</sub> with a mass ratio of 1:1 was used as air cathode material for Zn-air battery measurements. As shown in Figure 6A, the open circuit voltages of Zn-air batteries are 1.47 V and 1.36 V for air cathode materials of Fe/Fe<sub>2</sub>O<sub>3</sub>@Fe-N-C-1000 and Pt/C+RuO<sub>2</sub>, respectively. Apparently, the Zn-air battery made from Fe/Fe<sub>2</sub>O<sub>3</sub>@Fe-N-C-1000 exhibits higher open circuit voltage than that of Zn-air battery assembled with commercial Pt/C+RuO<sub>2</sub>. At a current density of 10 mA cm<sup>-2</sup>, the galvanostatic discharge

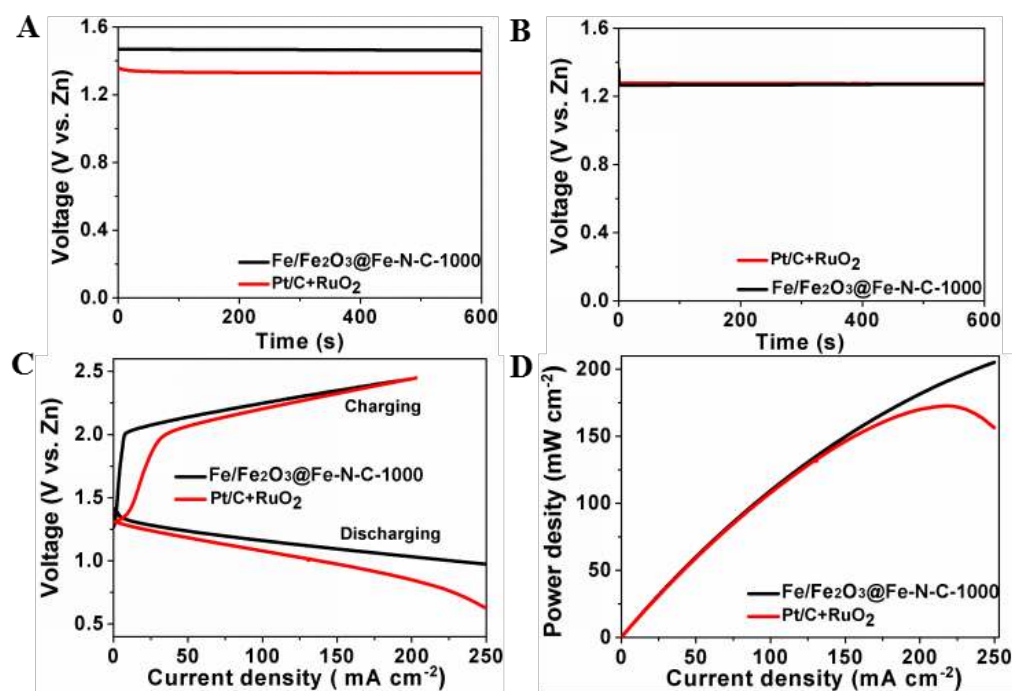


**Figure 6** (A) Open circuit voltage measurements of Zn-air batteries with Fe/Fe<sub>2</sub>O<sub>3</sub>@Fe-N-C-1000 and Pt/C+RuO<sub>2</sub> as the cathode catalysts. (B) Typical galvanostatic discharge curves of Zn-air batteries with Fe/Fe<sub>2</sub>O<sub>3</sub>@Fe-N-C-1000 and Pt/C+RuO<sub>2</sub> as cathode catalysts at 10 mA cm<sup>-2</sup>. (C) Discharge and charge polarization curves of rechargeable Zn-air batteries with different electrocatalysts. (D) Power density plots of Zn-air batteries with different electrocatalysts.

measurements demonstrate that the performance of Zn-air battery assembled with  $\text{Fe}/\text{Fe}_2\text{O}_3@\text{Fe-N-C-1000}$  is almost identical with Pt/C+ $\text{RuO}_2$ -based Zn-air battery (Figure 6B). Under given experimental conditions, the discharge voltage can almost keep at 1.28 V for both Zn-air batteries assembled with  $\text{Fe}/\text{Fe}_2\text{O}_3@\text{Fe-N-C-1000}$  and Pt/C+ $\text{RuO}_2$ . Figure 6C shows the performance of rechargeable Zn-air batteries based on  $\text{Fe}/\text{Fe}_2\text{O}_3@\text{Fe-N-C-1000}$  and Pt/C+ $\text{RuO}_2$ . The results demonstrate that in the charging process, the charging current densities of Zn-air batteries based on  $\text{Fe}/\text{Fe}_2\text{O}_3@\text{Fe-N-C-1000}$  and Pt/C+ $\text{RuO}_2$  can achieve 81 mA cm<sup>-2</sup> and 103 mA cm<sup>-2</sup> at a charging voltage of 2.2 V, respectively. Obviously, the charging performance of Zn-air battery assembled with Pt/C+ $\text{RuO}_2$  is lightly better than that of Zn-air battery based on  $\text{Fe}/\text{Fe}_2\text{O}_3@\text{Fe-N-C-1000}$ . However, the discharging current density (218 mA cm<sup>-2</sup>) of Zn-air battery based on  $\text{Fe}/\text{Fe}_2\text{O}_3@\text{Fe-N-C-1000}$  at 1.0 V is significantly higher than that (138 mA cm<sup>-2</sup>) of Zn-air battery assembled with Pt/C+ $\text{RuO}_2$  at the same voltage, indicating an excellent discharging performance of Zn-air battery based on  $\text{Fe}/\text{Fe}_2\text{O}_3@\text{Fe-N-C-1000}$  owing to its superior ORR catalytic activity. The corresponding power density curves of Zn-air batteries assembled with  $\text{Fe}/\text{Fe}_2\text{O}_3@\text{Fe-N-C-1000}$  and Pt/C+ $\text{RuO}_2$  are shown in Figure 6D. As shown, the power density of Zn-air battery based on  $\text{Fe}/\text{Fe}_2\text{O}_3@\text{Fe-N-C-1000}$  is still enhanced in the range of the investigated current density, while the power density of Zn-air battery assembled with Pt/C+ $\text{RuO}_2$  achieves a maximum value (173 mW cm<sup>-2</sup> at 0.79 V) at current density of 220 mA cm<sup>-2</sup>, obviously smaller than that (193 mW cm<sup>-2</sup> at 1.0 V) of Zn-air battery based on  $\text{Fe}/\text{Fe}_2\text{O}_3@\text{Fe-N-C-1000}$  at the same current density. Also, it is found that the morphology of  $\text{Fe}/\text{Fe}_2\text{O}_3@\text{Fe-N-C-1000}$  has no obvious change after five charging-discharging cycling (Figure S5 in the ESM), indicating its high stability in alkaline electrolyte as air cathode catalyst in rechargeable Zn-air battery. The above results clearly demonstrate that  $\text{Fe}/\text{Fe}_2\text{O}_3@\text{Fe-N-C-1000}$  is a high-performance bifunctional oxygen electrocatalyst (ORR activity responsible for

discharging process and OER activity responsible for charging process) with great potential as air cathode material for rechargeable Zn-air battery. The superior ORR catalytic activity of  $\text{Fe}/\text{Fe}_2\text{O}_3@\text{Fe-N-C-1000}$  compared to commercial Pt/C and  $\text{RuO}_2$  catalysts contributes its high discharging performance in rechargeable Zn-air battery, while slightly lower OER catalytic activity of  $\text{Fe}/\text{Fe}_2\text{O}_3@\text{Fe-N-C-1000}$  compared to commercial  $\text{RuO}_2$  catalyst results in its decreased charging performance in rechargeable Zn-air battery. Even so, the  $\text{Fe}/\text{Fe}_2\text{O}_3@\text{Fe-N-C-1000}$  exhibits great application potential in rechargeable Zn-air battery in comparison with commercial Pt/C+ $\text{RuO}_2$  catalyst owing to its low cost, source abundance, high stability and superior functionality of ORR and OER.

In this work, we cannot provide direct evidences to confirm the origins of ORR and OER catalytic activities of  $\text{Fe}/\text{Fe}_2\text{O}_3@\text{Fe-N-C-1000}$ . However, the reported theoretical and experimental results have verified that N doping and Fe, N doping in carbon structures can effectively create catalytic active sites for ORR [4, 21, 25, 28]. Moreover, recent reports also demonstrate that  $\text{Fe}@\text{Fe}_x\text{O}_y$  core-shell nanoparticles anchored on Fe, N doped carbon structures will not change the ORR catalytic mechanism, but effectively promote the ORR performance [22, 39]. Recently, the work reported by Bao *et al.* indicates that high-density iron nanoparticles encapsulated within N-doped carbon nanoshells possess superior bifunctional electrocatalytic activities toward both ORR and OER, exhibiting high performance and cycling stability as air cathode materials for rechargeable Zn-air batteries [2]. Based on the above discussion, the superior bifunctional ORR and OER activities of  $\text{Fe}/\text{Fe}_2\text{O}_3@\text{Fe-N-C-1000}$  may be attributed to a synergistic contribution of Fe, N doping and  $\text{Fe}/\text{Fe}_2\text{O}_3$  nanoparticles in graphitic carbon, promising as a candidate for rechargeable Zn-air batteries.

## 4 Conclusions

In summary,  $\text{Fe}/\text{Fe}_2\text{O}_3$  nanoparticles anchored on

Fe-N-doped carbon nanosheets ( $\text{Fe}/\text{Fe}_2\text{O}_3@/\text{Fe-N-C}$ ) were successfully fabricated using shrimp-shell derived N-doped carbon nanodots as low-cost, abundant carbon and nitrogen sources in the presence of  $\text{FeCl}_3$  by a simple pyrolysis approach. The experimental results demonstrated that  $\text{Fe}/\text{Fe}_2\text{O}_3@/\text{Fe-N-C-1000}$  possessed mesoporous structure and high surface area, as electrocatalyst exhibiting superior bifunctional catalytic activities toward both ORR and OER. This provided an opportunity to use  $\text{Fe}/\text{Fe}_2\text{O}_3@/\text{Fe-N-C-1000}$  as air cathode material for rechargeable Zn-air battery. The results demonstrated that the Zn-air battery assembled with  $\text{Fe}/\text{Fe}_2\text{O}_3@/\text{Fe-N-C-1000}$  exhibited high performance and durability. Our work would be valuable to design and develop low-cost and abundant non-precious metal contained N-doped carbon materials as bifunctional oxygen electrocatalysts for rechargeable Zn-air batteries.

### Acknowledgements

This work was financially supported by the Natural Science Foundation of China (Grant No. 51372248 and 51432009), the Instrument Developing Project of the Chinese Academy of Sciences (Grant No. yz201421) and the CAS/SAFEA International Partnership Program for Creative Research Teams of Chinese Academy of Sciences, the CAS Pioneer Hundred Talents Program and the Users with Potential Program (2015HSC-UP006, Hefei Science Center, CAS), China.

**Electronic Supplementary Material:** Supplementary material (TEM image and EFTEM element mapping images of  $\text{Fe}/\text{Fe}_2\text{O}_3@/\text{Fe-N-C-1000}$ , EDS, TG and BET characterizations of the samples, electrochemical durability and crossover effect measurements of electrocatalysts) is available in the online version of this article at [http://dx.doi.org/10.1007/s12274-\\*\\*\\*-\\*\\*\\*\\*-](http://dx.doi.org/10.1007/s12274-***-****-)

### References

- [1] Li, Y. G.; Dai, H. J. Recent advances in zinc-air batteries. *Chem. Soc. Rev.* **2014**, *43*, 5257-5275.
- [2] Wang, J.; Wu, H. H.; Gao, D. F.; Miao, S.; Wang, G. X.; Bao, X. H. High-density iron nanoparticles encapsulated within nitrogen-doped carbon nanoshell as efficient oxygen electrocatalyst for zinc-air battery. *Nano Energy* **2015**, *13*, 387-396.
- [3] Li, Y. G.; Gong, M.; Liang, Y. Y.; Feng, J.; Kim, J. E.; Wang, H. L.; Hong, G. S.; Zhang, B.; Dai, H. J. Advanced zinc-air batteries based on high-performance hybrid electrocatalysts. *Nat. Commun.* **2013**, *4*, 1805-1811.
- [4] Wu, Z. Y.; Xu, X. X.; Hu, B. C.; Liang, H. W.; Lin, Y.; Chen, L. F.; Yu, S. H. Iron carbide nanoparticles encapsulated in mesoporous Fe-N-Doped carbon nanofibers for efficient electrocatalysis. *Angew. Chem. Int. Ed.* **2015**, *54*, 8179-8183.
- [5] Lee, J. S.; Park, G. S.; Kim, S. T.; Liu, M. L.; Cho, J. A. Highly efficient electrocatalyst for the oxygen reduction reaction: N-doped ketjenblack incorporated into  $\text{Fe}/\text{Fe}_3\text{C}$ -functionalized melamine foam. *Angew. Chem. Int. Ed.* **2013**, *125*, 1060-1064.
- [6] Zhang, J. T.; Zhao, Z. H.; Xia, Z. H.; Dai, L. M. A metal-free bifunctional electrocatalyst for oxygen reduction and oxygen evolution reactions. *Nat. Nanotechnol.* **2015**, *10*, 444-452.
- [7] Jiang, H. L.; Yao, Y. F.; Zhu, Y. H.; Liu, Y. Y.; Su, Y. H.; Yang, X. L.; Li, C. Z. Iron carbide nanoparticles encapsulated in mesoporous Fe-N-doped graphene-like carbon hybrids as efficient bifunctional oxygen electrocatalysts. *ACS Appl. Mater. Interface* **2015**, *7*, 21511-21520.
- [8] Wu, G.; Zelenay, P. Nanostructured nonprecious metal catalysts for oxygen reduction reaction. *ACS Chem. Res.* **2013**, *46*, 1878-1889.
- [9] Xu, J. Y.; Aili, D.; Li, Q. F.; Christensen, E.; Jensen, J. O.; Zhang, W.; Hansen, M. K.; Liu, G. Y.; Wang, X. D.; Bjerrum, N. J. Oxygen evolution catalysts on supports with a 3-D ordered array structure and intrinsic proton



- conductivity for proton exchange membrane steam electrolysis. *Energy Environ. Sci.* **2014**, *7*, 820-830.
- [10.] Cheng, F. Y.; Chen, J. Metal-air batteries: from oxygen reduction electrochemistry to cathode catalysts. *Chem. Soc. Rev.* **2012**, *41*, 2172-2192.
- [11] Jaouen, F.; Proietti, E.; Lefèvre, M.; Chenitz, R.; Dodelet, J.-P.; Wu, G.; Chung, H. T.; Johnston, C. M.; Zelenay, P. Recent advances in non-precious metal catalysis for oxygen-reduction reaction in polymer electrolyte fuel cells. *Energy Environ. Sci.* **2011**, *4*, 114-130.
- [12] Dai, L. M.; Xue, Y. H.; Qu, L.; Choi, H.-J.; Baek, J.-B. Metal-free catalysts for oxygen reduction reaction. *Chem. Rev.* **2015**, *115*, 4823-4892.
- [13] Liang, Y. Y.; Li, Y. G.; Wang, H. L.; Zhou, J. G.; Wang, J.; Regier, T.; Dai, H. J. Co<sub>3</sub>O<sub>4</sub> nanocrystals on graphene as a synergistic catalyst for oxygen reduction reaction. *Nat. Mater.* **2011**, *10*, 780-786.
- [14] Fan, X. J.; Peng, Z. W.; Ye, R. Q.; Zhou, H. Q.; Guo, X. M<sub>3</sub>C (M: Fe, Co, Ni) nanocrystals encased in graphene nanoribbons: an active and stable bifunctional electrocatalyst for oxygen reduction and hydrogen evolution reactions. *ACS nano* **2015**, *9*, 7407-7418.
- [15] Lin, L.; Zhu, Q.; Xu, A. W. Noble-metal-free Fe-N/C catalyst for highly efficient oxygen reduction reaction under both alkaline and acidic conditions. *J. Am. Chem. Soc.* **2014**, *136*, 11027-11033.
- [16] Peng, H. L.; Mo, Z. Y.; Liao, S. J.; Liang, H. G.; Yang, L. J.; Luo, F.; Song, H. Y.; Zhong, Y. L.; Zhang, B. Q. High performance Fe- and N- doped carbon catalyst with graphene structure for oxygen reduction. *Scientific reports* **2013**, *3*, 1765-1771.
- [17] Deng, D. H.; Yu, L.; Chen, X. Q.; Wang, G. X.; Jin, L.; Pan, X. L.; Deng, J.; Sun, G. Q.; Bao, X. H. Iron encapsulated within pod-like carbon nanotubes for oxygen reduction reaction. *Angew. Chem. Int. Ed.* **2013**, *52*, 371-375.
- [18] Wu, Z.-S.; Yang, S. B.; Sun, Y.; Parvez, K.; Feng, X. L.; Müllen, K. 3D nitrogen-doped graphene aerogel-supported Fe<sub>3</sub>O<sub>4</sub> nanoparticles as efficient electrocatalysts for the oxygen reduction reaction. *J. Am. Chem. Soc.* **2012**, *134*, 9082-9085.
- [19] Huang, J. J.; Zhu, N. W.; Yang, T. T.; Zhang, T. P.; Wu, P. X.; Dang, Z. Nickel oxide and carbon nanotube composite (NiO/CNT) as a novel cathode non-precious metal catalyst in microbial fuel cells. *Biosens. Bioelectron.* **2015**, *72*, 332-339.
- [20] Wu, T. X.; Zhang, H. M.; Zhang, X.; Zhang, Y. X.; Zhao, H. J.; Wang, G. Z. A low-cost cementite (Fe<sub>3</sub>C) nanocrystal@ N-doped graphitic carbon electrocatalyst for efficient oxygen reduction. *Phys. Chem. Chem. Phys.* **2015**, *17*, 27527-27533.
- [21] Jia, Q. Y.; Ramaswamy, N.; Hafiz, H.; Tylus, U.; Strickland, K.; Wu, G.; Barbiellini, B.; Bansil, A.; Holby, E. F.; Zelenay, P.; Mukerjee, S. Experimental observation of redox-induced Fe-N switching behavior as a determinant role for oxygen reduction activity. *ACS Nano* **2015**, *9*, 12496-12505.
- [22] Huang, D. K.; Luo, Y. P.; Li, S. H.; Wang, M. K.; Shen, Y. Hybrid of Fe@Fe<sub>3</sub>O<sub>4</sub> core-shell nanoparticle and iron-nitrogen-doped carbon material as an efficient electrocatalyst for oxygen reduction reaction. *Electrochim. Acta.* **2015**, *174*, 933-939.
- [23] Cao, R. G.; Thapa, R.; Kim, H.; Xu, X. D.; Kim, M. G.; Li, Q.; Park, N.; Liu, M. L.; Cho, J. Promotion of oxygen reduction by a bio-inspired tethered iron phthalocyanine carbon nanotube-based catalyst. *Nat. Commun.* **2013**, *4*, 2076-2082.
- [24] Zhu, C. Z.; Zhai, J. F.; Dong, S. J. Bifunctional fluorescent carbon nanodots: green synthesis via soy milk and application as metal-free electrocatalysts for oxygen reduction. *Chem. Commun.* **2012**, *48*, 9367-9369.
- [25] Zhang, H. M.; Wang, Y.; Wang, D.; Li, Y. B.; Liu, X. L.; Liu, P.; Yang, H. G.; An, T. C.; Tang, Z. Y.; Zhao, H. J. Hydrothermal transformation of dried grass into graphitic carbon-based high performance electrocatalyst for oxygen reduction reaction. *Small* **2014**, *10*, 3371-3378.

- [26] Zhang, H. M.; Chen, J. Y.; Li, Y. B.; Liu, P. R.; Wang, Y.; An, T. C.; Zhao, H. J. Nitrogen-doped carbon nanodots@nanospheres as an efficient electrocatalyst for oxygen reduction reaction. *Electrochim. Acta.* **2015**, *165*, 7-13.
- [27] Liu, R. R.; Zhang, H. M.; Liu, S. W.; Zhang, X.; Wu, T. X.; Ge, X.; Zang, Y. P.; Zhao, H.; Wang, G. Z. Shrimp-shell derived carbon nanodots as carbon and nitrogen sources to fabricate three-dimensional N-doped porous carbon electrocatalysts for oxygen reduction reaction. *Phys. Chem. Chem. Phys.* **2016**, *18*, 4095-4101.
- [28] Gong, K. P.; Du, F.; Xia, Z. H.; Durstock, M.; Dai, L. M. Nitrogen-doped carbon nanotube arrays with high electrocatalytic activity for oxygen reduction. *Science* **2009**, *323*, 760-764.
- [29] Qu, L. T.; Liu, Y.; Baek, J.-B.; Dai, L. M. Nitrogen-doped graphene as efficient metal-free electrocatalyst for oxygen reduction in fuel cells. *ACS Nano* **2010**, *4*, 1321-1326.
- [30] Li, Y. B.; Zhang, H. M.; Wang, Y.; Liu, P. R.; Yang, H. G.; Yao, X. D.; Wang, D.; Tang, Z. Y.; Zhao, H. J. A self-sponsored doping approach for controllable synthesis of S and N co-doped trimodal-porous structured graphitic carbon electrocatalysts. *Energy Environ. Sci.* **2014**, *7*, 3720-3726.
- [31] Liang, J.; Jiao, Y.; Jaroniec, M.; Qiao, S. Z. Sulfur and nitrogen dual-doped mesoporous graphene electrocatalyst for oxygen reduction with synergistically enhanced performance. *Angew. Chem., Int. Ed.* **2012**, *51*, 11496-11500.
- [32] Liang, H. W.; Wei, W.; Wu, Z. S.; Feng, X. L.; Müllen, K. Mesoporous metal-nitrogen-doped carbon electrocatalysts for highly efficient oxygen reduction reaction. *J. Am. Chem. Soc.* **2013**, *135*, 16002-16005.
- [33] Teng, X. W.; Black, D.; Watkins, N. J.; Gao, Y. L.; Yang, H. Platinum-maghemite core-shell nanoparticles using a sequential synthesis. *Nano Lett.* **2003**, *3*, 261-264.
- [34] Zhao, Y.; Watanabe, K.; Hashimoto, K. Self-supporting oxygen reduction electrocatalysts made from a nitrogen-rich network polymer. *J. Am. Chem. Soc.* **2012**, *134*, 19528-19531.
- [35] Liu, S. W.; Wang, X. B.; Zhao, H. J.; Cai, W. P. Micro/nano-scaled carbon spheres based on hydrothermal carbonization of agarose. *Colloid. Surf. A* **2015**, *484*, 386-393.
- [36] Liu, R. L.; Wu, D. Q.; Feng, X. L.; Mullen, K. Nitrogen-doped ordered mesoporous graphitic arrays with high electrocatalytic activity for oxygen reduction. *Angew. Chem. Int. Ed.* **2010**, *49*, 2565-2569.
- [37] Yang, W. X.; Liu, X. J.; Yue, X. Y.; Jia, J. B.; Guo, S. J. Bamboo-like carbon nanotube/Fe<sub>3</sub>C nanoparticle hybrids and their highly efficient catalysis for oxygen reduction. *J. Am. Chem. Soc.* **2015**, *137*, 1436-1439.
- [38] Gorlin, Y.; Jaramillo, T. F. A Bifunctional Nonprecious Metal Catalyst for Oxygen Reduction and Water Oxidation. *J. Am. Chem. Soc.* **2010**, *132*, 13612-13614.
- [39] Tylus, U.; Jia, Q. Y.; Strickland, K.; Ramaswamy, N.; Serov, A.; Atanassov, P.; Mukerjee, S. Elucidating oxygen reduction active sites in pyrolyzed metal-nitrogen coordinated non-precious-metal electrocatalyst systems. *J. Phys. Chem. C* **2014**, *118*, 8999-9008.